Research Article Vol. 30, No. 15 / 18 Jul 2022 / Optics Express 26534
Optics EXPRESS

Flexible passive integrated photonic devices with superior optical and mechanical performance

YE LUO,[1,2,3] CHUNLEI SUN,[2,3] HUI MA,[4,5] MAOLIANG WEI,[4,5] JUNYING LI,[4,5] JIALING JIAN,[2,3] CHUYU ZHONG,[4,5] ZEQUN CHEN, RENJIE TANG,[2,3] KATHLEEN A. RICHARDSON,[6] HONGTAO LIN,[4,5] AND LAN LI[2,3,*]

[1]*Zhejiang University, Hangzhou 310027, China*
[2]*Key Laboratory of 3D Micro/Nano Fabrication and Characterization of Zhejiang Province, School of Engineering, Westlake University, Hangzhou 310024, China*
[3]*Institute of Advanced Technology, Westlake Institute for Advanced Study, Hangzhou 310024, China*
[4]*State Key Laboratory of Modern Optical Instrumentation, College of Information Science and Electronic Engineering, Zhejiang University, Hangzhou 310027, China*
[5]*MOE Frontier Science Center for Brain Science & Brain-Machine Integration, Zhejiang University, Hangzhou 310027, China*
[6]*The College of Optics & Photonics, Department of Materials Science & Engineering, University of Central Florida, Orlando, FL 32816, USA*
[*]*lilan@westlake.edu.cn*

Abstract: Flexible integrated photonics is a rapidly emerging technology with a wide range of possible applications in the fields of flexible optical interconnects, conformal multiplexing sensing, health monitoring, and biotechnology. One major challenge in developing mechanically flexible integrated photonics is the functional component within an integrated photonic circuit with superior performance. In this work, several essential flexible passive devices for such a circuit were designed and fabricated based on a multi-neutral-axis mechanical design and a monolithic integration technique. The propagation loss of the waveguide is calculated to be 4.2 dB/cm. In addition, we demonstrate a microring resonator, waveguide crossing, multimode interferometer (MMI), and Mach–Zehnder interferometer (MZI) for use at 1.55 μm, each exhibiting superior optical and mechanical performance. These results represent a significant step towards further exploring a complete flexible photonic integrated circuit.

1. Introduction

Integrated photonic devices have attracted extensive research attention in optical communication [1,2], sensing [3–5], 3D imaging [6], and life science applications [7,8] due to their large bandwidth and multiplexing capability, large integration capacity, strong optical confinement for enhanced light-matter interactions, and excellent immunity to electromagnetic interference. With the development of integrated photonics and nanofabrication technologies on flexible substrates, flexible integrated photonics has become a new frontier research field, showing great potential in a broader range of applications [9], including chip-to-chip optical interconnects [10,11], conformal and implantable sensing [12–19], broadband photonic tuning [20,21], and optogenetic stimulation and phototherapy [19,22].

A complete flexible integrated photonic circuit consists of various functional components, including active devices such as light sources [23], amplifiers, modulators, and detectors [24], as well as passive devices such as propagating waveguides, resonators, crossings, and interferometers. Previous studies have focused on mechanically flexible passive waveguides and resonators, but

#464896 https://doi.org/10.1364/OE.464896
Journal © 2022 Received 24 May 2022; revised 28 Jun 2022; accepted 28 Jun 2022; published 7 Jul 2022

Optics EXPRESS

the research on the active components integrated onto flexible platforms has been seldomly reported [24–30]. One scheme for manufacturing flexible photonic devices was developed based on polymeric materials with excellent intrinsic flexibility and stretchability [23,29–32]. However, the low refractive index contrast between the polymer waveguide core and cladding layers does not offer freedom in designing and fabricating compact optical structures for strong optical confinement [32,33]. Silicon-based inorganic materials, conventionally deposited under high-temperature plasma gas, present challenges towards achieving high-performance photonic devices directly on soft polymer substrates [25]. Recently, flexible and stretchable low-loss waveguides and microresonators have been demonstrated based on chalcogenide glasses (ChGs), which are amorphous optical materials exhibiting wide infrared transparency ranges, high refractive indices, and strong nonlinearities [14,15,24]. Their amorphous nature and compatibility with low-temperature film deposition methods allow monolithic integration on a flexible polymer substrate, making ChGs a promising material platform for flexible photonic devices.

In this work, we demonstrate a series of flexible passive ChG photonic devices at 1.55 μm using a combination of the monolithic integration technique and multi-neutral-axis mechanical design, including waveguide crossings, multimode interferometers (MMI), and Mach–Zehnder interferometers (MZI), which have not been investigated based on a high-index contrast material platform. Despite conventional fabrication techniques for flexible devices, including photolithography [15], nanoimprinting [34], and ink-jet printing [35,36], we choose to use electron-beam lithography (EBL) [14,37] for flexible photonic device fabrication, considering EBL's advantages in high resolution and alignment accuracy. The finite element method (FEM) software was used to calculate the strain distribution between layers and determine the position of the neutral axis. A transmission loss of 4.2 dB/cm for waveguides (800 nm width and 450 nm height) was calculated from measurements on microring resonators (MRRs) with an intrinsic quality factor of around 1.0×10^5. The obtained waveguide crossing at 1.55 μm showed an insertion loss of 0.11 dB. We also designed, fabricated, and characterized other passive devices, including the MMI and MZI. These passive devices were repeatedly bent down to a sub-millimeter radius without measurable degradation in optical performance and could be potentially used for constructing a complete flexible photonic integrated circuit.

2. Structure and design

Device structures have been optimized to achieve extreme mechanical robustness by employing a multi-neutral-axis mechanical design. Figure 1(a) shows the cross-sectional layer structure of our flexible passive integrated photonic devices. Due to its excellent mechanical property, chemical resistance, optical transparency and biocompatibility, a negative photoresist (SU-8) was used as the polymer bottom and top cladding layers [38]. The core layer of the device was made of $Ge_{23}Sb_7S_{70}$ (GSS), which is one type of ChG with superior oxidation resistance, a low optical loss, and a large refractive index (around 2.26 at 1550 nm) [39]. To release the device from its rigid handler substrate while preserving its integrity, we use a double-layer tape consisting of 25-μm-thick silicone and 20-μm-thick polyimide as the mechanical supporting layer. When the multilayer structure is subject to pure bending, there is a neutral plane where the strain remains zero in the SU-8 layer. Figure 1(b) shows the neutral axis position within different SU-8 layer thicknesses calculated by the Finite element method (FEM). The area on the right of the dashed line represents the position of the neutral axis within the SU-8 layer. To ensure the integrity of the passive device during the transfer process, we choose the SU-8 thickness of 20 μm, and the red pentacle in Fig. 1(b) indicates the position of the device's neutral axis. Figure 1(c) shows the simulated strain distribution using FEM when the bending radius is 1 mm. The simulation results reveal that the peak strain inside the passive device layer is no more than 1%, and the device placed close to the neutral plane possesses even less strain upon different bending radii

Optics EXPRESS

(Fig. 1(d)). Thus, the optical performance of our fabricated passive photonic devices should remain almost unchanged with a sub-millimeter bending radius.

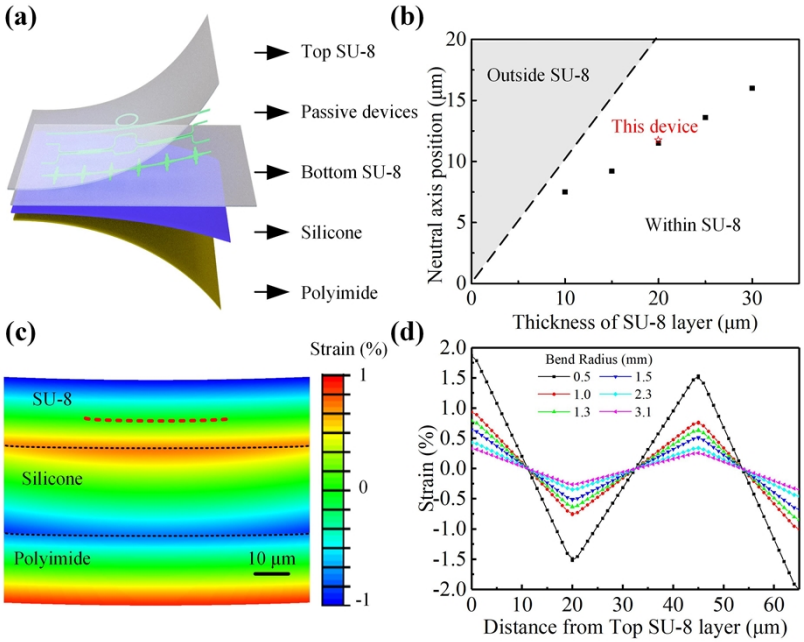

Fig. 1. (a) Laminated structure of the flexible passive device. (b) Neutral axis position from SU-8 layer surface as a function of the SU-8 thickness. The dashed line denotes the boundary of the SU-8 layer. (c) Contour plot of the FEM strain distribution in the device under a bent condition (bending radius: 1 mm). The black dashed line denotes the boundary of different layers. The Red dashed line indicates the position of the devices. (d) Strain distribution in the flexible passive device with a SU-8 layer thickness of 20 μm at different bending radii.

3. Fabrication and measurement

The fabrication process employed for our passive devices is shown in Fig. 2. Firstly, a commercial silicon wafer with 500 nm thermal oxide was used as a handler substrate. Then SU-8 photoresist was spin-coated onto the substrate as the bottom cladding of the photonic device. The following 450 nm GSS film was deposited by thermal evaporation at a relatively low temperature, which could avoid damaging the organic substrate. Then a 50 nm silicon oxide layer was sputtered onto the sample to prevent the etching of GSS by an alkaline developer. Next, we patterned the device by EBL (Raith VOYAGER, Dortmund, Germany) using the EBL photoresist (maN 2403). We etched the sample by inductively coupled plasma (Leuven Inc., Xuzhou, China) using a fluorine-based atmosphere (CF_4: CHF_3 = 1:3), whose selective etching ratio is 1:4. The sample was then cladded by another 7 μm SU-8. Finally, the sample was immersed in Hydrogen Fluoride solution (HF, 40%) to etch the silicon oxide sacrificial layer before a layer of double-sided tape was applied to support the free-standing film structures.

A home-built setup illustrated in Fig. 3(a) was used to characterize the optical performance of the fabricated devices. The light launched from the tunable laser (Santec Inc., Komaki, Japan, 1 pm resolution in the range of 1260–1620 nm) was first adjusted by the polarization controller before being coupled into the device under test (DUT) through a vertical coupling system. The two ends of the flexible device were mounted to a couple of linear motion stages, as shown in

Optics EXPRESS

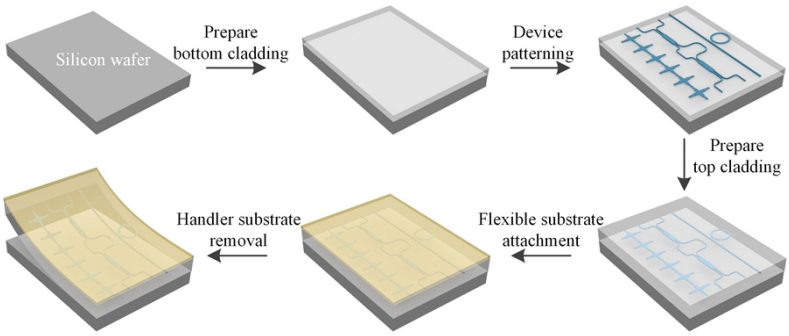

Fig. 2. Fabrication process flow of the flexible passive photonic devices.

Fig. 3(b). The compression strain applied to the membrane was controlled by changing the distance between the two motion stages. The inset of Fig. 3(b) shows the optical microscope image of the grating coupler (GC). The DUT, connected with focusing grating couplers by two straight waveguides, was placed in the middle of the two stages. A polynomial fit method was used to fit the side view of the curved flexible device to attain the bending radius. The device's transmission spectrum was obtained under different bending radii and bending cycles to validate their optical and mechanical performance.

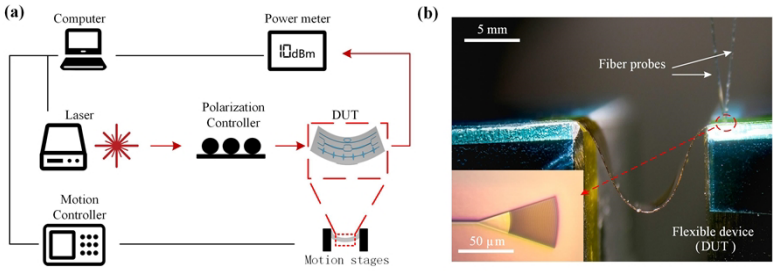

Fig. 3. (a) Schematic diagram of the device characterization setup. (b) Photo of a flexible sample during the measurement; the inset is the microscope photo of the focusing grating coupler).

The waveguide width was chosen as 800 nm to maintain the single-mode condition. We designed and fabricated the 450 nm fully etched focusing GC with a coupling angle of 8 deg. The GC has a period of 1.01 μm and a duty cycle of 0.5 and presents a coupling loss of 6.3 dB at 1600 nm.

4. Results and discussion

The scanning electron microscopy (SEM) image of the MRR is shown in the inset of Fig. 4(a). The ring diameter is 50 μm, and the gap between the coupling waveguide and the ring is 450 nm. The transmission spectrum of MRR is shown in Fig. 4(b). The ring was operated in the under coupling regime, and their free spectral range (FSR) is about 3.194 nm. The intrinsic quality factor (Q_i) is as high as 1.3×10^5. And an average Q_{in} of (1 ± 0.2) 10^5 was demonstrated, corresponding to an equivalent optical propagation loss of 4.2 dB/cm, compatible with previously published results [15,39–46].

Since the MRRs were placed close to the neutral plane, the shifts in the resonance dips in the transmission spectra were not easily detected with decreasing bending radius, as shown in

Optics EXPRESS

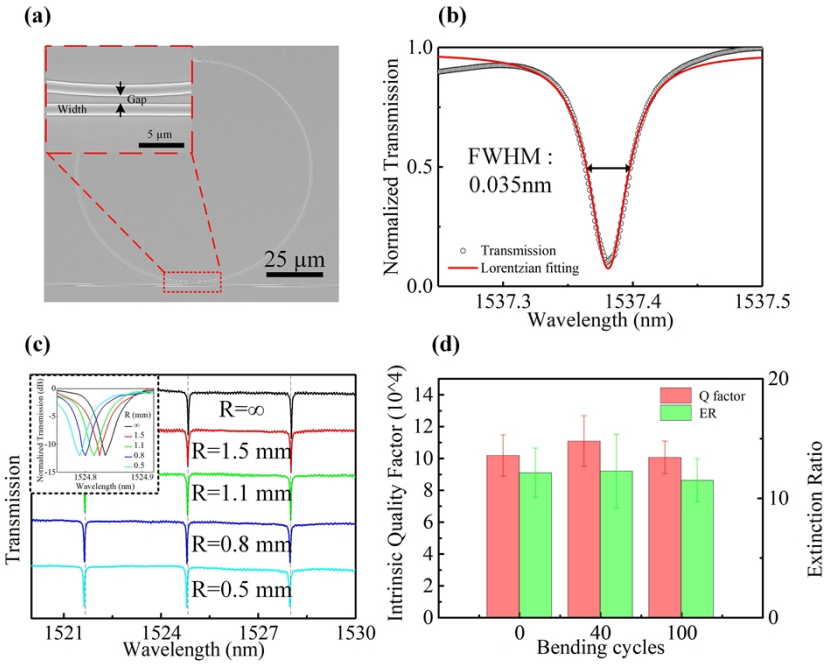

Fig. 4. (a) SEM image of the MRR (Top-view); inset shows the magnified area of the gap between the bus waveguide and the MRR. (b) Transmission spectrum of an MRR and its Lorentzian fitting curve. (c) Transmission spectrum of the MRR at different bending radii, inset shows the transmission spectrum at a wavelength of around 1525 nm under different bending radii. (d) Q-factors and extinction ratios of the MRR after multiple bending cycles at a radius of 0.5 mm.

Fig. 4(c). When the MRR is under a bending radius of 0.5 mm, the resonance wavelength shift is 50 pm at 1525 nm, corresponding to a strain of −0.16%. The MRR's optical characteristics are measured after repeated bending cycles, as shown in Fig. 4(d). the bending radius is down to 0.5 mm. The quality factors and the extinction ratios of MRR remain minimal variations after multiple bending cycles.

However, an MRR alone is not enough to construct a complete flexible photonic circuit; there are a number of other indispensable passive components that have not been demonstrated based on a high-index contrast material platform, including waveguide crossings, MMIs, and MZIs.

Waveguide crossings play an essential role in routing and splitting optical power in a photonic network [47,48]. We designed and fabricated the flexible waveguide crossing with low insertion loss and high mechanical stability for the first time. The crossing is composed of two orthogonal 1×1 MMIs with a total size of 9.4 μm × 2.0 μm (length × width). As shown in Fig. 5(a), several critical parameters, including L_T, L_M, and W_M were optimized to be 2.2 μm, 3.6 μm, and 2.0 μm, respectively. The transmission spectra and spatial mode field distribution are shown in Fig. 5(b), indicating a small crosstalk without obvious reflection and radiation at the intersection region. And the insertion loss of waveguide crossings was calculated to be 0.11 ± 0.01 dB (Fig. 5(c)) for a single waveguide crossing at 1550 nm via testing different numbers of the cascading units (Fig. 5(a)). We also recorded the transmission spectra of the waveguide crossing before and after 100 cycles of bending at a radius of 0.5 mm. As shown in Fig. 5(d), the acceptable variations in the insertion loss of the single waveguide crossing indicate the device's superior mechanical stability.

Optics EXPRESS

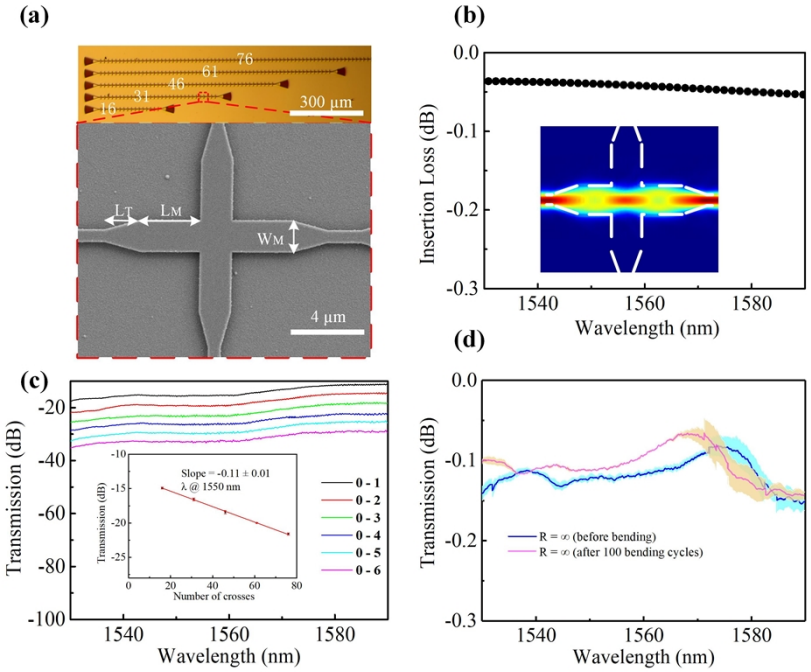

Fig. 5. (a) Optical and SEM images of the fabricated waveguide crossing. (b) Simulated insertion loss and electric field distribution of the optimized device excited with a quasi-TE mode polarization. (c) Insertion loss measurements of the waveguide crossing. (d) Transmission spectrum of the waveguide crossing before and after 100 cycles of bending at a radius of 0.5 mm. The solid lines correspond to average transmittance through the waveguide crossing. The shaded regions denote the standard deviation of the transmittance due to coupling variation.

The MMI is another commonly used basic building block as an optical splitter, filter, coupler, and combiner in a flexible photonic system attributed to its advantages of compact size, large bandwidth and large fabrication tolerance [49,50]. We optimized the flexible 2×2 MMI with a total size of 76.2 μm × 7.2 μm (length × width) based on the self-imaging theory and a 3D Finite Difference Time Domain (Lumerical FDTD software) simulation method. As shown in Fig. 6(a), several critical parameters, including W_1, W_2, W_M, L_M and T_M were determined to be 4.5 μm, 2.1 μm, 7.2 μm, 46.2 μm, and 15 μm, respectively. The simulated electric field distribution of the mode profile for the optimized MMI is shown in Fig. 6(b)., indicating a low crosstalk at the input and uniform power splitting at the output. And the insertion loss was calculated to be 3.42 ± 0.07 dB for an MMI at 1550 nm (Fig. 6(c)) via measuring the cascaded structures from port 0 to ports 1–6 (Fig. 6(a)).We also measured the optical performance of the MMI after 100 bending cycles at a radius of 0.5 mm as shown in Fig. 6(d). There were minimal variations in the insertion loss of a single MMI over a broad wavelength range, demonstrating the similarly excellent mechanical performance.

We also designed and fabricated the imbalanced flexible MZI. They are usually used to vary the relative phase shift between two beams, which is an important function applied in passive filters and routers, and active devices such as modulators, detectors and isolators [51–53]. As shown in Fig. 7(a), the imbalanced MZI consists of two 2×2 MMIs connected by two bent waveguide arms with a bending radius of 50 μm to avoid radiation loss. And the relative phase delay is induced by the 200 μm length difference between the two arms of the MZI. As a result,

Optics EXPRESS

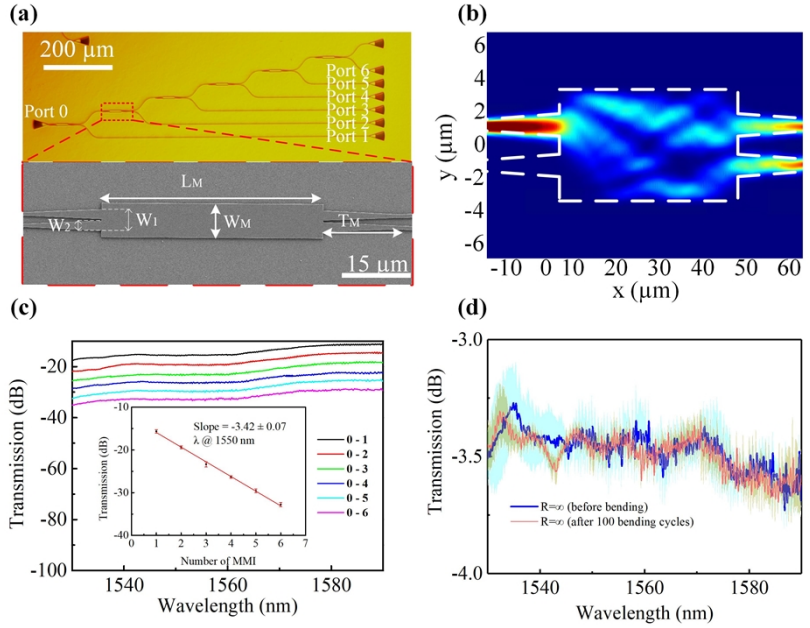

Fig. 6. (a) Optical and SEM images of the fabricated MMI. (b) Simulated electric field distribution of the optimized device excited with a quasi-TE mode polarization. (c) Insertion loss measurements of the MMI. (d) Transmission spectrum of the MMI before and after 100 cycles of bending at a radius of 0.5 mm. The solid lines correspond to average transmittance through the MMI. The shaded regions denote the standard deviation of the transmittance due to coupling variation.

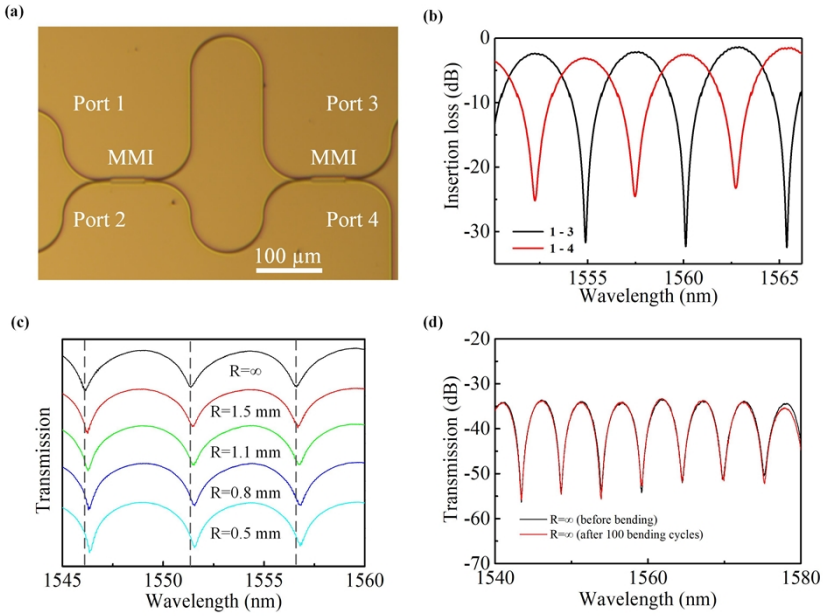

Fig. 7. (a) Optical image of the fabricated MZI. (b) Insertion loss of the MZI circuit measured at its two output ports. (c) The shift of the interference fringes in the output of the MZI at different bending radii. (d) Transmission spectra of the MZI before and after 100 cycles of bending at a radius of 0.5 mm.

Optics EXPRESS

an insertion loss of less than 1 dB and extinction ratios of over 20 dB was achieved in Fig. 7(b). The obtained transmission spectra also exhibit equal power splitting between the two output ports. To validate the mechanical performance of the MZIs, the flexible MZI's optical characteristics were measured upon different bending radii (Fig. 7(c)) and after repeated bending cycles with a bending radius of 0.5 mm (Fig. 7(d)). The thickness variation in the SU-8 layers might shift the position of the neutral-axis plane, resulting in a slight shift in the resonance dips with decreasing bending radius.

5. Conclusion

We have designed, fabricated, and characterized flexible passive photonic devices by combining a multi-neutral-axis mechanical design and a monolithic integration technique, including several basic photonic units, including MRRs, waveguide crossing, MMIs and MZIs. The equivalent propagation loss of the flexible waveguide inferred from a ring resonator was 4.2 dB/cm. For the first time, flexible high-index contrast waveguide crossings, MMIs and MZIs were demonstrated with an insertion loss of less than 0.11 dB, 3.42 dB, and 1 dB, respectively. The imbalanced MZI exhibits an extinction ratio greater than 20 dB. Guided by the multi-neutral axis theory, we have achieved passive photonic devices allowing efficient flexibility, despite the inherent mechanical fragility of the glass film. The devices can withstand significant bending upon sub-millimeter radii without compromising their optical performance. These passive devices could be critical functional units for a complete flexible photonic circuit, showing great potential in some emerging fields for flexible optical interconnect and epidermal sensing applications.

Funding. National Natural Science Foundation of China (62175202, 12104375, 61975179, 91950204); National Key Research and Development Program of China (2019YFB2203003); Leading Innovative and Entrepreneur Team Introduction Program of Zhejiang (2020R01005); Natural Science Foundation of Zhejiang Province (LD22F040002); Foundation of Westlake Multidisciplinary Research Initiative Center (MRIC103536022010).

Acknowledgments. The authors thank Westlake Center for Micro/Nano Fabrication and Instrumentation and Service Center for Physical Sciences at Westlake University and 2JU Micro-Nano Fabrication Center at Zhejiang University for the facility support. The authors would also like to thank Zihao Wang, Qing Zhao, and Liming Shan for their help in film preparation and characterization.

Disclosures. The authors declare no conflicts of interest.

Data availability. Data underlying the results presented in this paper are not publicly available at this time but may be obtained from the authors upon reasonable request.

References

1. R Zhang, Y He, Y Zhang, S An, Q Zhu, X Li, and Y Su, "Ultracompact and low-power-consumption silicon thermo-optic switch for high-speed data," Nanophotonics **10**(2), 937–945 (2020).
2. S Ummethala, T Harter, K Koehnle, Z Li, S Muehlbrandt, Y Kutuvantavida, J Kemal, P Marin-Palomo, J Schaefer, A Tessmann, S K Garlapati, A Bacher, L Hahn, M Walther, T Zwick, S Randel, W Freude, and C Koos, "THz-to-optical conversion in wireless communications using an ultra-broadband plasmonic modulator," Nat. Photonics **13**(8), 519–524 (2019).
3. W J Westerveld, M Mahmud-Ul-Hasan, R Shnaiderman, V Ntziachristos, X Rottenberg, S Severi, and V Rochus, "Sensitive, small, broadband and scalable optomechanical ultrasound sensor in silicon photonics," Nat. Photonics **15**(5), 341–345 (2021).
4. Y Hazan, A Levi, M Nagli, and A Rosenthal, "Silicon-photonics acoustic detector for optoacoustic micro-tomography," Nat. Commun. **13**(1), 1488 (2022).
5. C Sun, C Zhong, M Wei, H Ma, Y Luo, Z Chen, R Tang, J Jian, H Lin, and L Li, "Free-spectral-range-free filters with ultrawide tunability across the S + C + L band," Photonics Res. **9**(6), 1013–1018 (2021).
6. C Rogers, A Y Piggott, D J Thomson, R F Wiser, I E Opris, S A Fortune, A J Compston, A Gondarenko, F Meng, X Chen, G T Reed, and R Nicolaescu, "A universal 3D imaging sensor on a silicon photonics platform," Nature **590**(7845), 256–261 (2021).
7. A Mohanty, Q Li, M A Tadayon, S P Roberts, G R Bhatt, E Shim, X C Ji, J Cardenas, S A Miller, A Kepecs, and M Lipson, "Reconfigurable nanophotonic silicon probes for sub-millisecond deep-brain optical stimulation," Nat. Biomed. Eng. **4**(2), 223–231 (2020).

Optics EXPRESS

8. A T Mashayekh, T Klos, D Geuzebroek, E Klein, T Veenstra, M Büscher, F Merget, P Leisching, and J Witzens, "Silicon nitride PIC-based multi-color laser engines for life science applications," Opt. Express **29**(6), 8635–8653 (2021).
9. S Geiger, J Michon, S Liu, J Qin, J Ni, J Hu, T Gu, and N Lu, "Flexible and Stretchable Photonics: The Next Stretch of Opportunities," ACS Photonics **7**(10), 2618–2635 (2020).
10. L Li, Y Zou, H T Lin, J J Hu, X C Sun, N N Feng, S Danto, K Richardson, T Gu, and M Haney, "A Fully-Integrated Flexible Photonic Platform for Chip-to-Chip Optical Interconnects," J. Lightwave Technol. **31**(24), 4080–4086 (2013).
11. L Jiang, A Nishant, J Frish, T S Kleine, L Brusberg, R Himmelhuber, K J Kim, J Pyun, S Pau, R A Norwood, and T L Koch, "SmartPrint Single-Mode Flexible Polymer Optical Interconnect for High Density Integrated Photonics," J. Lightwave Technol. **40**(12), 3839–3844 (2022).
12. J Xiao, T Zhou, N Yao, S Ma, C Pan, P Wang, H Fu, H Liu, J Pan, L Yu, S Wang, W Yang, L Tong, and L Zhang, "Optical fibre taper-enabled waveguide photoactuators," Nat. Commun. **13**(1), 363 (2022).
13. H Bai, S Li, J Barreiros, Y Tu, C R Pollock, and R F Shepherd, "Stretchable distributed fiber-optic sensors," Science **370**(6518), 848–852 (2020).
14. L Li, H T Lin, S T Qiao, Y Z Huang, J Y Li, J Michon, T Gu, C Alosno-Ramos, L Vivien, A Yadav, K Richardson, N S Lu, and J J Hu, "Monolithically integrated stretchable photonics," Light: Sci. Appl. **7**(1), 8 (2018).
15. L Li, H T Lin, S T Qiao, Y Zou, S Danto, K Richardson, J D Musgraves, N S Lu, and J J Hu, "Integrated flexible chalcogenide glass photonic devices," Nat. Photonics **8**(8), 643–649 (2014).
16. G H Lee, H Moon, H Kim, G H Lee, W Kwon, S Yoo, D Myung, S H Yun, Z Bao, and S K Hahn, "Multifunctional materials for implantable and wearable photonic healthcare devices," Nat. Rev. Mater. **5**(2), 149–165 (2020).
17. W Bai, H Yang, Y Ma, H Chen, J Shin, Y Liu, Q Yang, I Kandela, Z Liu, S-K Kang, C Wei, C R Haney, A Brikha, X Ge, X Feng, P V Braun, Y Huang, W Zhou, and J A Rogers, "Flexible Transient Optical Waveguides and Surface-Wave Biosensors Constructed from Monocrystalline Silicon," Adv. Mater. **30**(32), 1801584 (2018).
18. J J Guo, M X Niu, and C X Yang, "Highly flexible and stretchable optical strain sensing for human motion detection," Optica **4**(10), 1285–1288 (2017).
19. J W Reddy, M Lassiter, and M Chamanzar, "Parylene photonics: a flexible, broadband optical waveguide platform with integrated micromirrors for biointerfaces," Microsyst. Nanoeng. **6**(1), 85–206 (2020).
20. T-W Lu, L-C Wang, C-H Lai, and P-T Lee, "Strain shapes the light in a photonic crystal nanocavity," Photonics Res. **8**(1), 24–31 (2020).
21. C L Yu, H Kim, N de Leon, I W Frank, J T Robinson, M McCutcheon, M Z Liu, M D Lukin, M Loncar, and H Park, "Stretchable Photonic Crystal Cavity with Wide Frequency Tunability," Nano Lett. **13**(1), 248–252 (2013).
22. Z Chen and L Li, "Flexible Photonic Probes for New-Generation Brain–Computer Interfaces," Acc. Mater. Res. **2**(5), 315–318 (2021).
23. S Chen, M-P Zhuo, X-D Wang, G-Q Wei, and L-S Liao, "Optical waveguides based on one-dimensional organic crystals," PhotoniX **2**(1), 2 (2021).
24. L Li, H T Lin, Y Z Huang, R J Shiue, A Yadav, J Y Li, J Michon, D Englund, K Richardson, T Gu, and J J Hu, "High-performance flexible waveguide-integrated photodetectors," Optica **5**(1), 44–51 (2018).
25. L Fan, L T Varghese, Y Xuan, J Wang, B Niu, and M Qi, "Direct fabrication of silicon photonic devices on a flexible platform and its application for strain sensing," Opt. Express **20**(18), 20564–20575 (2012).
26. Y Chen, H Li, and M Li, "Flexible and tunable silicon photonic circuits on plastic substrates," Sci. Rep. **2**(1), 622 (2012).
27. L Li, P Zhang, W M Wang, H T Lin, A B Zerdoum, S J Geiger, Y C Liu, N Xiao, Y Zou, O Ogbuu, Q Y Du, X Q Jia, J J Li, and J J Hu, "Foldable and Cytocompatible Sol-gel TiO2 Photonics," Sci. Rep. **5**(1), 13832 (2015).
28. A V Shneidman, K P Becker, M A Lukas, N Torgerson, C Wang, O Reshef, M J Burek, K Pau, J McLellan, and M Loncar, "All-Polymer Integrated Optical Resonators by Roll-to-Roll Nanoimprint Lithography," ACS Photonics **5**(5), 1839–1845 (2018).
29. H J Zuo, S L Yu, T Gu, and J J Hu, "Low loss, flexible single-mode polymer photonics," Opt. Express **27**(8), 11152–11159 (2019).
30. H T Lin, Y Song, and Y Z Huang, *et al.*, "Chalcogenide glass-on-graphene photonics," Nat. Photonics **11**(12), 798–805 (2017).
31. T Amemiya, T Kanazawa, T Hiratani, D Inoue, Z Gu, S Yamasaki, T Urakami, and S Arai, "Organic membrane photonic integrated circuits (OMPICs)," Opt. Express **25**(16), 18537–18552 (2017).
32. J Missinne, S Kalathimekkad, B Van Hoe, E Bosman, J Vanfleteren, and G Van Steenberge, "Stretchable optical waveguides," Opt. Express **22**(4), 4168–4179 (2014).
33. A Melloni, R Costa, G Cusmai, and F Morichetti, "The role of index contrast in dielectric optical waveguides," IJMPT **34**(4), 421–437 (2009).
34. C Zhang, H Subbaraman, Q C Li, Z Y Pan, J G Ok, T Ling, C J Chung, X Y Zhang, X H Lin, R T Chen, and L J Guo, "Printed photonic elements: nanoimprinting and beyond," J. Mater. Chem. C **4**(23), 5133–5153 (2016).
35. X Lin, T Ling, H Subbaraman, X Zhang, K Byun, L J Guo, and R T Chen, "Ultraviolet imprinting and aligned ink-jet printing for multilayer patterning of electro-optic polymer modulators," Opt. Lett. **38**(10), 1597–1599 (2013).
36. X H Lin, T Ling, H Subbaraman, L J Guo, and R T Chen, "Printable thermo-optic polymer switches utilizing imprinting and ink-jet printing," Opt. Express **21**(2), 2110–2117 (2013).

Optics EXPRESS

37. N Qin, Z G Qian, C Zhou, X X Xia, and T H Tao, "3D electron-beam writing at sub-15 nm resolution using spider silk as a resist," Nat. Commun. **12**(1), 5133 (2021).
38. J J Hu, V Tarasov, A Agarwal, L Kimerling, N Carlie, L Petit, and K Richardson, "Fabrication and testing of planar chalcogenide waveguide integrated microfluidic sensor," Opt. Express **15**(5), 2307–2314 (2007).
39. Q Y Du, Y Z Huang, J Y Li, D Kita, J Michon, H T Lin, L Li, S Novak, K Richardson, W Zhang, and J J Hu, "Low-loss photonic device in Ge-Sb-S chalcogenide glass," Opt. Lett. **41**(13), 3090–3093 (2016).
40. J Lapointe, Y Ledemi, S Loranger, V L Iezzi, E S de Lima, F Parent, S Morency, Y Messaddeq, and R Kashyap, "Fabrication of ultrafast laser written low-loss waveguides in flexible As2S3 chalcogenide glass tape," Opt. Lett. **41**(2), 203–206 (2016).
41. Z Yang, R Z Zhang, Z Y Wang, P P Xu, W Zhang, Z Kang, J J Zheng, S X Dai, R P Wang, and A Majumdar, "High-Q, submicron-confined chalcogenide microring resonators," Opt. Express **29**(21), 33225–33233 (2021).
42. X L Zhang, C F Zhou, Y Luo, Z Yang, W Zhang, L Li, P P Xu, P Q Zhang, and T F Xu, "High Q-factor, ultrasensitivity slot microring resonator sensor based on chalcogenide glasses," Opt. Express **30**(3), 3866–3875 (2022).
43. C F Zhou, X L Zhang, Y Luo, C Hou, Z Yang, W Zhang, L Li, P P Xu, and T F Xu, "Narrow-bandwidth Bragg grating filter based on Ge-Sb-Se chalcogenide glasses," Opt. Express **30**(8), 12228–12236 (2022).
44. Y Zhu, L Wan, Z S Chen, Z L Yang, D Xia, P Y Zeng, J C Song, J S Pan, Y M Feng, M J Zhang, W P Liu, J P Li, B Zhang, and Z H Li, "Effects of Shallow Suspension in Low-Loss Waveguide-Integrated Chalcogenide Microdisk Resonators," J. Lightwave Technol. **38**(17), 1 (2020).
45. J C Song, X J Guo, W T Peng, J S Pan, L Wan, T H Feng, S Q Zeng, D Liu, B Zhang, M J Zhang, and Z H Li, "Stimulated Brillouin Scattering in Low-Loss Ge25Sb10S65 Chalcogenide Waveguides," J. Lightwave Technol. **39**(15), 5048–5053 (2021).
46. H Y Shang, D D Sun, M J Zhang, J C Song, Z L Yang, D Liu, S Q Zeng, L Wan, B Zhang, Z Wang, Z H Li, and Y G Liu, "On-Chip Detector Based on Supercontinuum Generation in Chalcogenide Waveguide," J. Lightwave Technol. **39**(12), 3890–3895 (2021).
47. D G Chen, L Wang, Y G Zhang, X Hu, X Xiao, and S H Yu, "Ultralow Crosstalk and Loss CMOS Compatible Silicon Waveguide Star-Crossings with Arbitrary Included Angles," ACS Photonics **5**(10), 4098–4103 (2018).
48. C L Wu, Y H Lin, S P Su, B J Huang, C T Tsai, H Y Wang, Y C Chi, C I Wu, and G R Lin, "Enhancing Optical Non linearity in a Nonstoichiometric SiN Waveguide for Cross-Wavelength All-Optical Data Processing," ACS Photonics **2**(8), 1141–1154 (2015).
49. A E Klein, N Janunts, S Schmidt, S Bin Hasan, C Etrich, S Fasold, T Kaiser, C Rockstuhl, and T Pertsch, "Dual-SNOM investigations of multimode interference in plasmonic strip waveguides," Nanoscale **9**(20), 6695–6702 (2017).
50. S Paesani, M Borghi, S Signorini, A Mainos, L Pavesi, and A Laing, "Near-ideal spontaneous photon sources in silicon quantum photonics," Nat. Commun. **11**(1), 2505 (2020).
51. Y Tian, Y Zhao, S P Liu, Q Li, W Wang, J B Feng, and J Guo, "Scalable and compact photonic neural chip with low learning-capability-loss," Nanophotonics **11**(2), 329–344 (2022).
52. Y L Gui, B M Nouri, M Miscuglio, R Amin, H Wang, J B Khurgin, H Dalir, and V J Sorger, "100 GHz micrometer-compact broadband monolithic ITO Mach-Zehnder interferometer modulator enabling 3500 times higher packing density," Nanophotonics (2022).
53. H H Zhu, J Zou, H Zhang, Y Z Shi, S B Luo, N Wang, H Cai, L X Wan, B Wang, X D Jiang, J Thompson, X S Luo, X H Zhou, L M Xiao, W Huang, L Patrick, M Gu, L C Kwek, and A Q Liu, "Space-efficient optical computing with an integrated chip diffractive neural network," Nat Commun **13**(1), 1044 (2022).